---

**Article:**
Schnitzer, Barbara, Welkenhuysen, Niek, Leake, Mark Christian orcid.org/0000-0002-1715-1249 et al. (2 more authors) (2022) The effect of stress on biophysical characteristics of misfolded protein aggregates in living Saccharomyces cerevisiae cells. Experimental gerontology. 111755. ISSN 1873-6815

https://doi.org/10.1016/j.exger.2022.111755

---

# The effect of stress on biophysical characteristics of misfolded protein aggregates in living *Saccharomyces cerevisiae* cells

Barbara Schnitzer [1,2], Niek Welkenhuysen [1,2], Mark C. Leake [3,4], Sviatlana Shashkova [1,2,3,§], Marija Cvijovic [1,2]

February 11, 2022

corresponding authors: marija.cvijovic@chalmers.se and sviatlana.shashkova@gu.se
[1] Department of Mathematical Sciences, Chalmers University of Technology, 412 96 Gothenburg, Sweden
[2] Department of Mathematical Sciences, University of Gothenburg, 412 96 Gothenburg, Sweden
[3] Department of Physics, University of York, YO10 5DD York, UK
[4] Department of Biology, University of York, YO10 5DD York, UK
[§] Current address: Department of Physics, University of Gothenburg, 412 96 Gothenburg, Sweden

## Abstract

Aggregation of misfolded or damaged proteins is often attributed to numerous metabolic and neurodegenerative disorders. To reveal underlying mechanisms and cellular responses, it is crucial to investigate protein aggregate dynamics in cells. Here, we used super-resolution single-molecule microscopy to obtain biophysical characteristics of individual aggregates of a model misfolded protein ΔssCPY* labelled with GFP. We demonstrated that oxidative and hyperosmotic stress lead to increased aggregate stoichiometries but not necessarily the total number of aggregates. Moreover, our data suggest the importance of the thioredoxin peroxidase Tsa1 for the controlled sequestering and clearance of aggregates upon both conditions. Our work provides novel insights into the understanding of the cellular response to stress via revealing the dynamical properties of stress-induced protein aggregates.

**Keywords: stress-induced protein aggregation, super-resolution single-molecule microscopy, stoichiometry, diffusion, protein quality control**

## 1 Introduction

To ensure the proper functioning, cells possess a complex protein quality control (PQC) network to maintain protein homeostasis via regulating protein production, folding and degradation. However, various factors, such as environmental stress (heat shock, oxidative stress or UV/IR radiation) and ageing, can cause disbalance in proteostasis followed by chronic expression of incorrectly folded proteins leading to aggregate formation. These aggregates are often toxic and recognised as a hallmark of metabolic and neurodegenerative disorders, such as type II diabetes, cancer, and Parkinson's, Alzheimer's, Huntington's diseases [1–3].

In eukaryotic cells, as an initial response to harmful environment, misfolded proteins are recognised by small heat-shock proteins (sHsps) and concentrated into aggregates to prevent further interactions [4]. In yeast, upon $H_2O_2$-induced oxidative stress, besides sHsps, the Tsa1 thioredoxin peroxidase has been shown to be

essential in the isolation of damaged proteins [5]. This PQC response results in appearance of multiple inclusion bodies which further sequestered at specific sites including the juxtanuclear quality control site (JUNQ), the intranuclear quality control site (INQ) and the peripheral vacuole-associated insoluble protein deposit (IPOD) [6–8].

To study spatial distributions in relation to temporal control of aggregates, a number of model misfolding proteins has been developed [9]. Fluorescently-tagged, such protein constructs are an indispensable tool enabling direct tracking of aggregate formation and localisation by light microscopy. Standard epifluorescence microscopy, however, represents the average behaviour of the protein pool which results in loss of information concerning any molecular heterogeneity, and may ultimately lead to misinterpretations of the underlying physiological relevance of subpopulations of molecules [10]. Localisation-based super-resolved microscopy methods enable tracking individual molecules of the same type to reveal "hidden" subpopulations providing novel insights into protein behaviour hence determining more precise biological functions [11].

In this study, we utilised a bespoke super-resolution fluorescence microscopy setup Slimfield with single-molecule precision and millisecond time resolution [12] to follow stress-induced protein aggregates in living *Saccharomyces cerevisiae* budding yeast cells. Slimfield microscopy utilises a delimited, high intensity excitation field at the sample of a focused laser beam that is expanded to ∼10 microns width, and has been used in multiple microbial studies to investigate DNA replication and remodelling [13–17], photosynthesis [18], gene regulation [19], cell division [20, 21], as well as multicellular tissues involved in immunity [22, 23]. As a model protein, we used a ΔssCPY*-GFP construct, a cytoplasmic misfolded mutant version of the vacuolar enzyme carboxypeptidase Y [24] that has been shown to localise in both, JUNQ and IPOD [6]. We investigate biophysical characteristics of ΔssCPY*-GFP foci, such as molecular stoichiometry and mobility, to reveal new aspects of aggregate formation and regulation in response to changes in the extracellular microenvironment. Our study provides novel insights into understanding of cellular response to stress through characterisation of stress-induced protein aggregates behaviour.

# 2 Materials and Methods

## Yeast strains and media

Cells from frozen stocks were pregrown on a standard YPD medium (20 g/l Bacto Peptone, 10 g/l Yeast Extract, 20 g/l agar) supplemented with 2% glucose (w/v) at 30°C overnight. The ΔssCPY*-GFP plasmid was introduced into the yeast cells by the standard lithium acetate protocol (14) followed by plating the transformants onto the uracil-deficient Yeast Nitrogen Base (YNB) agar plates (1.7 g/l YNB w/o amino acids and w/o $NH_4SO_4$, 5 g/l $NH_4SO_4$, 2% (w/v) glucose, 1x amino acid supplement -ura, 20 g/l agar). A full list of strains used in this study is presented in Table 1.

| **Name** | **Genotype** | **Source** |
|---|---|---|
| Wild type | MAT **a** *his3Δ1 leu2Δ0 met15Δ0 ura3Δ pRS316-Myc-tsa1DYF* | Molin's lab |
| *tsa1Δ* | MAT **a** *his3Δ1 leu2Δ0 met15Δ0 ura3Δ tsa1D::kanMX4 pRS316-Myc-tsa1DYF* | Molin's lab |
| *TSA1OX* | MAT **alpha** *his3Δ1::pRS403-myc-TSA1, leu2Δ0 lys2Δ0 ura3Δ0* | [5] |
| TSA1 backbone | MAT **alpha** *his3Δ1::pRS403, leu2Δ0 lys2Δ0 ura3Δ0* | [5] |

**Table 1: List of yeast strains used in this study.**

For microscopy experiments, cells were pregrown overnight in YNB media at 30°C, 180 rpm, subcultured to $OD_{600}$ ∼0.2 and grown to mid-logarithmic phase. For oxidative and osmotic stress experiments, 0.4M (final concentration) $H_2O_2$ and 1M NaCl, respectively, were added to the cultures 1h prior to imaging. Cells were then immobilised by placing 5 µl of the cell culture onto a 1% agarose pad perfused with YNB supplemented with 1mM $H_2O_2$ or 0.5M NaCl. The pad with cells was then sealed with a plasma-cleaned BK7 glass coverslip.

## Single-molecule microscopy

Slimfield excitation was implemented via 50mW 488nm wavelength laser (Coherent Obis) de-expanded to direct a beam onto the sample at 10mW excitation intensity to observe single GFP in living yeast cells. Fluorescence emission was captured by 1.49 NA oil immersion objective lens (Nikon). Images were acquired at 5ms exposure time at 200 fps by the EMCCD camera (iXon DV860-BI, Andor technology, UK) camera using 80 nm/pixel magnification. Fluorescent spots, within the microscope depth of field were detected and quantified using a single particle tracking algorithm (example in Fig S1) with ∼40nm spatial precision [17], denoted as $\sigma$, adapted from similar studies reported previously [13]. The molecular stoichiometry of each spot was estimated using a step-wise photobleaching method, by dividing the summed pixel intensity value associated with the initial brightness of individual foci by the brightness of a single fluorescently-tagged molecule. Specifically, the initial unbleached intensity, I0, was determined using a heuristic exponential photobleach decay function [25]. The intensity corresponding to a single fluororophore, Isingle, was estimated from the end photobleach traces corresponding to the brightness of the last remaining photoactive fluorophore. We then determined the stoichiometry as I0/Isingle (described in detail in [19]). As detailed previously, the analysis code integrates all detected fluorescence intensity of tracked foci within the microscope's depth of field and does not vary significantly with height from the coverslip surface over this depth range equivalent to several hundred nanometres [17]. The apparent microscopic diffusion coefficient $D$ was determined for each track by calculating the initial gradient of the relation between the mean square displacement with respect to tracking time interval using the first 10 frames while constraining the linear fit to pass through $4\sigma^2$ on the vertical axis corresponding to a time interval value of zero. $4\sigma^2$ is the expected non-zero measured mean square displacement at zero time interval in the 2D plane of the camera detector due to this level of sampling uncertainty. The final data, underlying all figures, can be found in supplementary File S1.

## Statistical analysis

To analyse if distributions are significantly different, statistical testing has been applied. In particular, by applying one-sided tests, we examined if distributions shifted towards higher or lower values.
Note that the distributions of aggregate stoichiometry or diffusion coefficients are heavily skewed, thus normality cannot be assumed. Due to alterations in the tails of the distributions (Fig S2A-B), they neither follow a log-normal distribution. When comparing the distributions, we therefore used the Mann-Whitney U test, being a non-parametric test that does not require knowledge about the underlying distributions and aims at testing if two data sets result from the same distribution. Only the number of aggregates per cell can be considered normally distributed (Fig S2C). We therefore performed a Student's t-test in this case.
For each hypothesis that we tested, we corrected the one-sided significance level $\alpha = 0.05$ according to Bonferroni [26] to reduce the probability of type I errors:

$$\alpha_c = \frac{\alpha}{n},$$

with n being the number of comparison between data sets made for a given hypothesis. There are typically 7 comparisons across conditions ($n = 7$), only when comparing subpopulation within a data set $n = 10$. We consider a significant difference if the p-value $p \leq \alpha_c$ (marked with ***). To complement the increased type II error caused by the correction, we also state significance without correction ($p \leq \alpha$, marked with **). The resulting p-values of all comparisons are summarised in supplementary File S2.

# 3 Results

## Stress affects the distributions of aggregate stoichiometry and diffusion coefficient

To understand the effect of stress on protein aggregation, we analysed single-molecule fluorescence Slimfield super-resolution microscopy images of yeast cells expressing the GFP-tagged protein construct ΔssCPY* known to be misfolded (Fig 1A). It allowed us to study the aggregation of this protein in three conditions: (1) standard without any perturbations, (2) cells in oxidative stress exposed to 1mM hydrogen peroxide ($H_2O_2$), and (3) cells in salt stress exposed to 0.5M sodium chloride (NaCl). We aquired 1000 frames at the rate of 200 frames per second. By employing advanced image analysis and tracking algorithms [13, 17], we obtained characteristics of individual aggregates (spots or foci), such as the foci apparent stoichiometry ($S$), an estimated number of ΔssCPY*-GFP molecules per aggregate by normalising the fluorescent signal of the spot by the signal of one single ΔssCPY*-GFP, and the diffusion coefficient ($D$), an estimated mean-squared displacement of the spot over 4 frames. Each aggregate is further attributed to a cell, allowing us to compare the number of aggregates and their characteristics across cells. We analysed 30-33 cells in each condition.

In all microenvironments, we found that $S$ and $D$ of ΔssCPY*-GFP aggregates are distributed with a heavy weight on small and slow aggregates, and only comparably few aggregates can diffuse faster or reach larger stoichiometries than the main pool (Fig 1B-D). Furthermore, the two observables are correlated and aggregates with high $S$ more likely move with low $D$ (Fig 1B).

Both oxidative and salt stress affect those distributions compared to standard conditions. More specifically, the aggregate stoichiometries $S$ generally increase and the diffusion coefficients $D$ decrease when exposed to stress (Fig 1C-D). Even though the trends are the same in both stress conditions, we found that NaCl has a stronger effect on $S$, while $H_2O_2$ is more limiting on $D$. These shifts are also measurable when estimating the average aggregate stoichiometry $\overline{S}$ and diffusion coefficient $\overline{D}$ per cell (Fig 1F).

To better understand the differences between the conditions, we divided the data sets into immobile ($D < 0.3\mu m^2(s)^{-1}$) and fast ($D > 0.8\mu m^2(s)^{-1}$) aggregates (Fig S3A). Even though molecules moving with $D < 0.3\mu m^2(s)^{-1}$ are slow-diffusing in general, they can be considered immobile for our purpose [19, 27]. Similarly, we split the data into small ($S < 10$) and large ($S \geq 10$) aggregates. In that way, it was possible to attribute the increase in $S$ in oxidative stress to only immobile aggregates, while salt stress showed a significant effect on all aggregates regardless of their speed. Similarly, in salt stress only small aggregates differed in $D$, while in oxidative stress all aggregates are significantly slowed down independent of their size.

We further observed that there are more cells with a large number of aggregates in NaCl, compared to non-stressed conditions and $H_2O_2$ (Fig 1E).

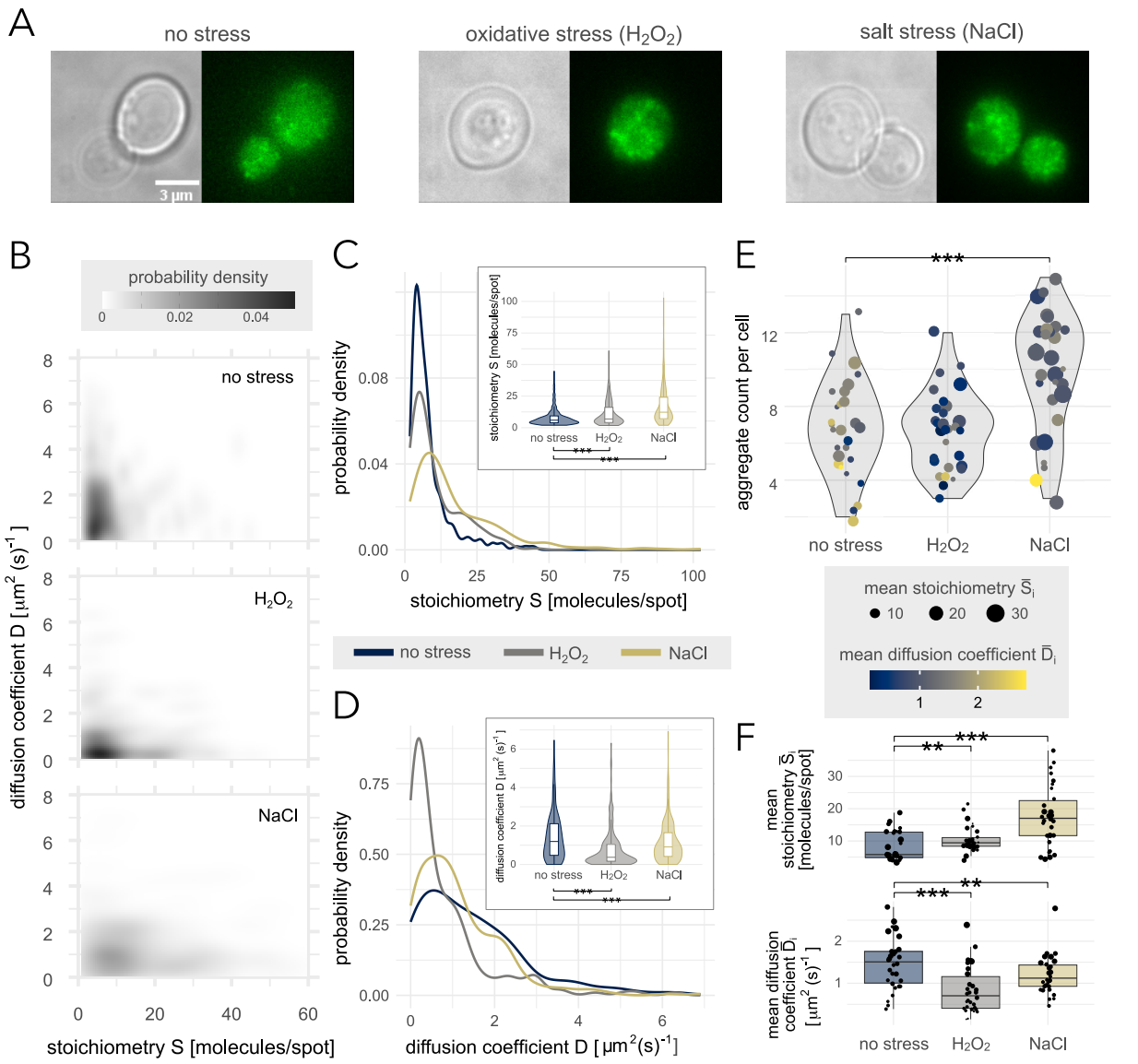


**Figure 1: Effect of $H_2O_2$ and NaCl on aggregate stoichiometry and mobility.** (A) Example microscopy images. (B) 2-d probability densities of the aggregate stoichiometry $S$ and the diffusion coefficient $D$. (C) 1-d probability densities of the aggregate stoichiometry $S$, with the corresponding distribution (violin with integrated boxplot) in the sub panel. The distributions shift towards larger aggregates compared to the control in standard conditions ($H_2O_2$ $p = 0.007$, NaCl $p < 0.0001$). (D) 1-d probability density of the aggregate diffusion coefficient $D$, with the corresponding distribution (violin with integrated boxplot) in the sub panel. The distributions shift towards slower aggregates compared to the control in standard conditions ($H_2O_2$ $p < 0.0001$, NaCl $p = 0.009$). (E) Distributions (violin plots) of the aggregate count per cell. Each point represents a cell, that has a mean aggregate stoichiometry (point size) and a mean aggregate diffusion coefficient (point color). In NaCl, there are more aggregates per cell ($p < 0.0001$). (F) Distributions (boxplots) of the aggregate stoichiometry $\overline{S}_i$ and the aggregate diffusion coefficient $\overline{D}_i$ of aggregates in cell $i$. Each data point represents a cell. The size of the point reflects the corresponding standard deviations. On average, cells have larger aggregates ($H_2O_2$ $p = 0.019$, NaCl $p < 0.0001$) with slower speed ($H_2O_2$ $p < 0.0001$, NaCl $p = 0.027$).

## Tsa1 deletion leads to shifts in the stoichiometries that can be attributed to fast aggregates

The thioredoxin peroxidase Tsa1 plays an important role for cells in dealing with damaged or misfolded proteins, particularly in oxidative stress conditions. Tsa1 is a hydrogen peroxide scavenger, that recruits heat shock proteins which together act as chaperones to aid the clearance of damaged proteins and protein aggregates [5, 6]. So far, no connection between Tsa1 and salt stress has been reported [28].

To test the role of Tsa1 in the protein aggregation process, we performed the same experiments described above with mutants lacking Tsa1 (*tsa1Δ*) and compared the results to the corresponding wildtype (wt). While the diffusion coefficients do not seem to be affected by the lack of Tsa1 in any microenvironment tested, the stoichiometry of the aggregates generally increases in standard and $H_2O_2$ conditions, but decreases in NaCl (Fig 2A-B, complemented by Fig S4). Also here, these trends could be confirmed when investigating the mean $\overline{S}$ and $\overline{D}$ in individual cells (Fig 2D). However, the changes were not as prominent anymore.

As before, we divided each data set into subpopulations and repeated the analysis to see if the deletion of Tsa1 affects immobile and fast aggregates in different ways (Fig S3B). The distributions, in general, do not depend on this separation into subpopulations, with two exceptions. When exposed to $H_2O_2$, we observed small differences in the distributions of $S$ between immobile and fast aggregates both in the wildtype and *tsa1Δ*. In the wildtype, fast aggregates typically correspond to low stoichiometries. The deletion of Tsa1 leads to a significant shift towards larger $S$ in the fast subpopulation, such that the difference between immobile and fast aggregates in the *tsa1Δ* strain is opposite to the wildtype. Fast aggregates in *tsa1Δ* are consequently typically larger than immobile ones. Even though, we could not find significant differences between the subpopulations in any other condition, we were in all microenvironments able to attribute the increase in $S$ caused by Tsa1 deletion to fast aggregates.

Investigating the difference between small and large aggregates did not lead to strong effects between the wildtype and *tsa1Δ* (Fig S3C). Interestingly, in oxidative stress there is a small decrease in $D$ only for small aggregates, which is not visible in the overall distributions. This can be a consequence of a shift of fast aggregates towards larger stoichiometries.

In $H_2O_2$, aggregates do not only tend to be larger without Tsa1, we also found more cells with a significantly increased number of aggregates compared to the wildtype (Fig 2C). In NaCl, in contrast, Tsa1 deletion leads to fewer spots per cell (Fig 2C), which moreover were shown to be smaller.

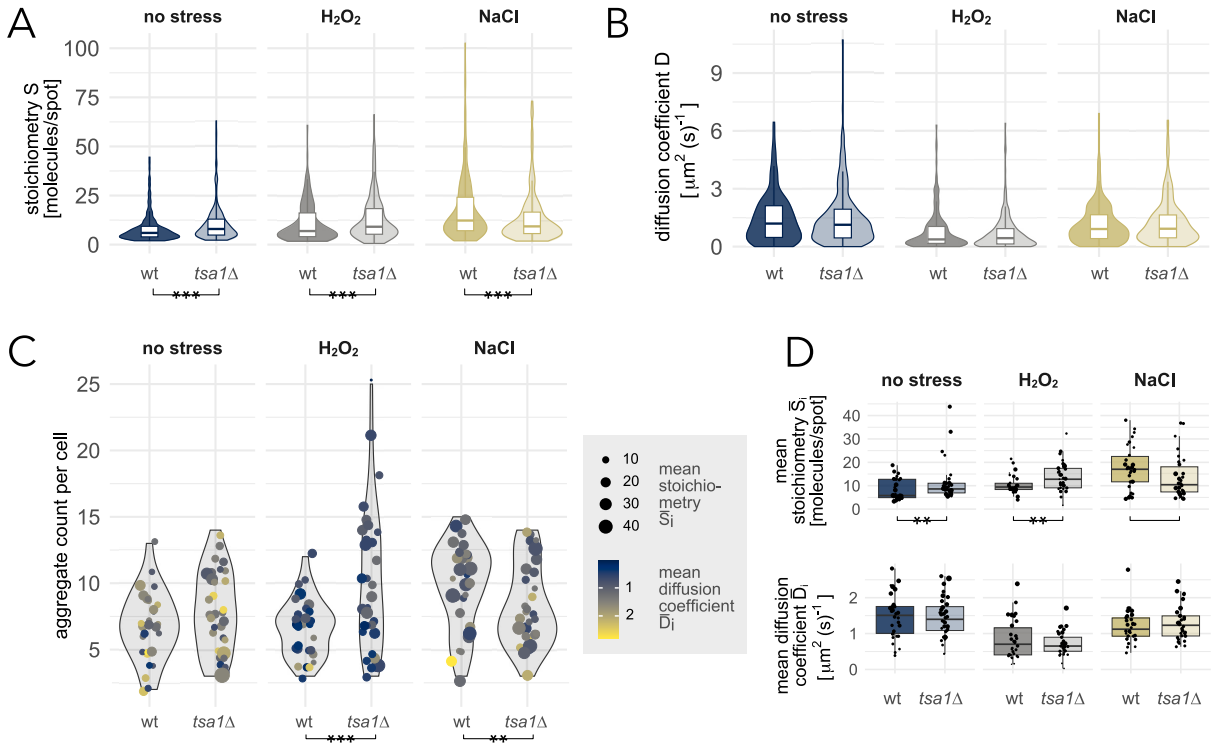


**Figure 2: Comparison between wildtype (wt) and Tsa1 deletion (*tsa1Δ*).** (A) Distributions (violin with integrated boxplot) of the aggregate stoichiometry $S$ for the wildtype and the *tsa1Δ* strain. *tsa1Δ* leads to a shift towards higher stoichiometry in standard conditions ($p < 0.0001$) and in $H_2O_2$ ($p = 0.003$), but towards lower stoichiometry in NaCl ($p < 0.0001$). (B) Distributions (violin with integrated boxplot) of the diffusion coefficient $D$ for the wildtype and the *tsa1Δ* strain. The diffusion coefficients are not significantly affected by the deletion of Tsa1. (C) Distributions (violin plots) of the aggregate counts per cell for the wildtype and the *tsa1Δ* strain. Each point represents a cell, that has a mean aggregate stoichiometry (point size) and a mean aggregate diffusion coefficient (point color). *tsa1Δ* leads to more aggregates per cell in $H_2O_2$ ($p = 0.0007$) and fewer in NaCl ($p = 0.029$). (D) Distributions (boxplots) of the mean stoichiometry $\overline{S}_i$ and the mean diffusion coefficient $\overline{D}_i$ of aggregates in cell $i$. Each data point represents a cell. The size of the point reflects the corresponding standard deviation. *tsa1Δ* slightly increases $\overline{S}$ in standard conditions ($p = 0.032$) and $H_2O_2$ ($p = 0.008$). In NaCl there is only a tendency towards smaller average stoichiometries (not significant, $p = 0.052$).

## Tsa1 overexpression leads to fewer but larger and slower aggregates in oxidative stress

To complement the Tsa1 deletion experiments, we also investigated the effect of Tsa1 overexpression (*TSA1OX*) (Fig 3, complemented by Fig S5). Since we obtained more significant differences for *tsa1Δ* in oxidative stress, we limited the analysis of *TSA1OX* to cells in standard conditions and under exposure to $H_2O_2$.

Similar to Tsa1 deletion, Tsa1 overexpression induces a shift in the distributions of $S$ towards larger numbers of ΔssCPY*-GFP molecules per spot in both conditions (Fig 3A and Fig S3D). This is also reflected in the average aggregate stoichiometry $\overline{S}$ in cells (Fig 3D).

*TSA1OX* further seems to have an effect on the distributions of the diffusion coefficients $D$ (Fig 3B). We observed a shift towards faster aggregates in standard conditions, but towards slower aggregates in $H_2O_2$. We could attribute these changes in $D$ to large aggregates with $S \geq 10$ (Fig S3E).

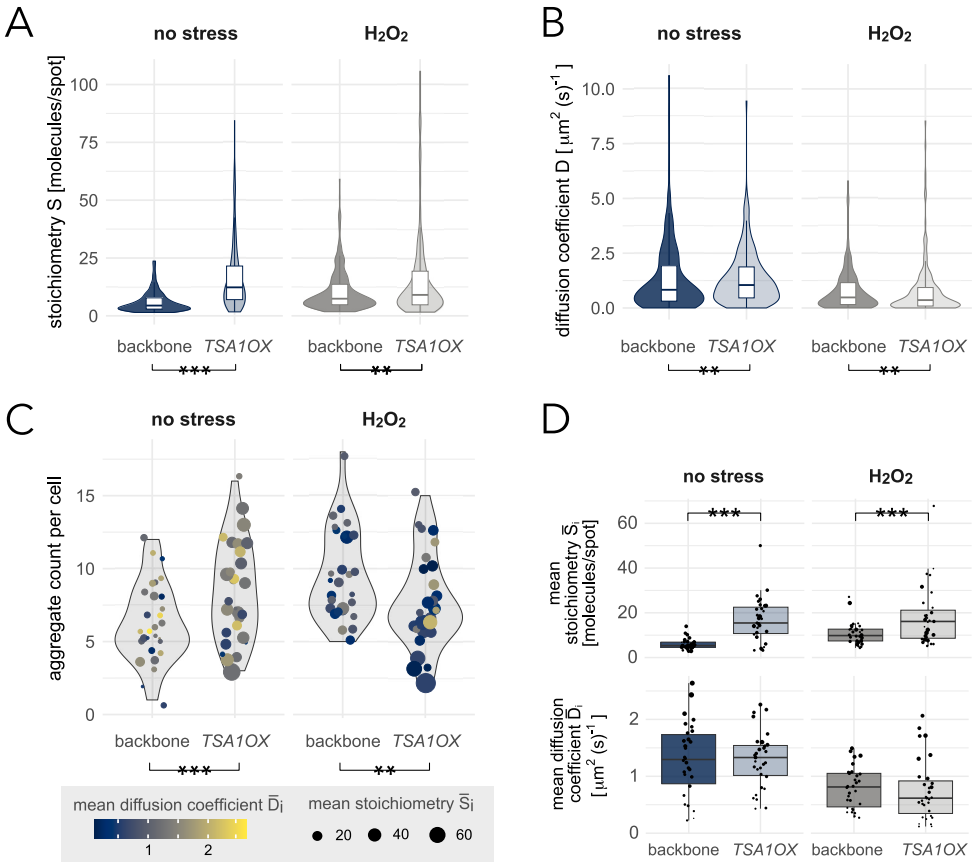


**Figure 3: Comparison between the backbone and Tsa1 overexpression (*TSA1OX*).** (A) Distributions (violin with integrated boxplot) of the aggregate stoichiometry $S$ for the backbone and the *TSA1OX* strain. *TSA1OX* leads to a shift towards higher stoichiometry (no stress $p < 0.0001$, $H_2O_2$ $p = 0.014$). (B) Distributions (violin with integrated boxplot) of the diffusion coefficient $D$ for the backbone and the *TSA1OX* strain. *TSA1OX* leads to a small shift towards faster aggregates in standard conditions ($p = 0.046$) and towards slower aggregates in $H_2O_2$ ($p = 0.039$). (C) Distributions (violin plots) of the aggregate counts per cell for the wildtype and the *TSA1OX* strain. Each point represents a cell, that has a mean aggregate stoichiometry (point size) and a mean aggregate diffusion coefficient (point color). *TSA1OX* leads to more aggregates per cell in standard conditions ($p = 0.003$) but decreased the number of aggregate per cell in $H_2O_2$ ($p = 0.016$). (D) Distributions (boxplots) of the mean stoichiometry $\overline{S}$ and the mean diffusion coefficient $\overline{D}$ of aggregates in cell $i$. Each data point represents a cell. The size of the point reflects the corresponding standard deviation. *TSA1OX* increases $\overline{S}$ (no stress $p < 0.0001$, $H_2O_2$ $p = 0.003$).

In addition, Tsa1 overexpression leads to a higher number of aggregates per cell in standard conditions, but when exposed to $H_2O_2$, reduces the counts compared to the respective backbone, such that the latter distribution is similar to non-stressed conditions again (Fig 3C). This is contrary to *tsa1Δ* where there were many more cells with a higher amount of aggregates (Fig 2C).

## Tsa1 is involved in limiting the maximal diffusion of aggregates

All effects measured earlier are based on changes in distributions, or means as summarising measures. Especially for *TSA1OX* (e.g. Fig 3A and D), we observed differences in the distributions of large aggregates, which typically are much fewer and therefore have minor effects on the overall distributions. Still, they seem to shape the 2-d distributions of the data (Fig 1B, S4A and S5A). More specific, we observed a correlation between the number of proteins per spot and the largest measured diffusion coefficients. The larger the

aggregate the more restricted its maximal observed mobility is. According to the Stokes-Einstein relation in viscous fluids, the diffusion coefficient $D$ of a particle is inversely proportional to its radius $r$. However, it was previously shown that the dependence *in vivo* can be stronger than $r^{-1}$ up to $r^{-6}$ [29–31]. In order to quantify the radius scaling dependence on $D$ in our data, we converted the number of proteins $S$ of each aggregate to a minimal volume $V$ $[nm^3]$ and thus minimal aggregate radius $r$ $[nm]$ under the assumption of a perfect sphere, based on [32]:

$$V = 1.212 \cdot 10^{-3} \cdot M \cdot S \tag{1}$$

$$r = \left(\frac{3V}{4\pi}\right)^{\frac{1}{3}}, \tag{2}$$

with the molecular mass of an individual ΔssCPY*-GFP protein construct estimated to $M = 84.66kDa$ [33]. Subsequently, we reduced each data set to its maximal diffusion coefficients (Fig 4A and Fig S6A). In our case, dividing the data into 10 bins along $r > 4.5nm$ and choosing the 5 data points with maximal $D$ per bin turned out to be a good representation. We then used the estimated radii of the reduced data sets together with the respective diffusion coefficients to fit the function $D(r) \propto r^c$, $c < 0$, applying least-squared fitting. Note that the transformation of the data to log-log scale simplifies the fitting to a line with slope $c$ (Fig S6B).

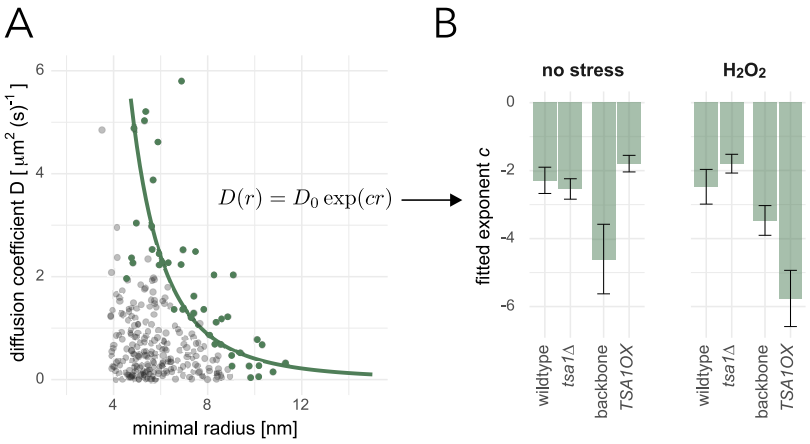


**Figure 4: Exponential fit to highest diffusion constants.** (A) Example data set with a reduced data set marked in green, consisting of the maximal measured diffusion coefficients per radius interval (conversion from $S$ to minimal radius $r$ according to (1) and (2)). The reduced data set is used for fitting the function $D(r)$. All fits are presented in Fig S6. (B) Fitted exponents $c$ for all data sets. *TSA1OX* has the largest effect on the highest diffusion coefficients.

In accordance with the literature, we obtained in all cases $1 < |c| < 6$ indicating a stronger dependence of the diffusion coefficient on the radius of the aggregate than the Stokes-Einstein relation suggests (Fig 4B). *TSA1OX* exhibits the most striking differences. In standard condition without stress, Tsa1 overexpression leads to the decrease of $|c|$ by more than one half. This means a weaker dependence of $D$ on $r$, allowing higher diffusion coefficients especially for large aggregates. In contrast, the exponent $|c|$ increases by approximately 70% for *TSA1OX* in oxidative stress compared to the backbone, indicating that aggregates with increasing stoichiometry are more limited in their mobility.
While deletion of Tsa1 shows opposite trends compared to the overexpression both in standard condition and under oxidative stress, the differences are too small to be considered significant.

# 4 Discussion

In this work, we utilised single-molecule super-resolution fluorescence microscopy Slimfield to gain insights into the stoichiometries ($S$) and diffusion coefficients ($D$) of individual protein aggregates, and their behaviour in different conditions. We used the protein construct ΔssCPY*-GFP as an example and tested the effects of oxidative or salt stress conditions, known to trigger protein misfolding and irreversible protein damage [34, 35]. We investigated differences between data sets of up to 33 cells per condition and in most cases, our data suggested that the analysis of the stoichiometries or the diffusion coefficients of all aggregates at once is a good representation of the respective average properties in a cell.

By correlating the two characteristics, we saw an inhibiting effect of the stoichiometry on the diffusion coefficient, which is physically reasonable given the increased mass of larger aggregates, that has to result in lower velocities, assuming that the underlying kinetic energy of the aggregate is limited by a constant temperature. Specifically, we could show that the highest measured diffusion coefficients of aggregates are dependent on the size of the aggregate following an inverse power law ($D \propto r^c, -6 < c < -1$), which confirms previously estimated relations [29–31].

The fitted exponents $c$ were based on the ideal assumption that an aggregate arranges as a perfect sphere with radius $r$. In reality, aggregates are likely to have a larger surface area due to imperfections in the shape. Moreover, some misfolded proteins, such as alpha-synuclein and Tau associated with Parkinson's and Alzheimer's diseases, respectively, can aggregate in a form of fibrils [36, 37]. Therefore, the radius $r$ estimated here is generally an underestimation of the real radius or cross section, or $D$ is an overestimation.

Interestingly, most aggregates diffuse significantly slower than the relation defined by $D(r) = D_0 r^c$ in all conditions. That most aggregates are not able to move that fast can be an effect of the high molecular density within cells, i.e. macromolecular crowding, inhibiting the mobility of aggregates [38, 39]. The reduction in $D$ could also be a direct consequence of the spatial PQC system, that actively controls aggregation mobility [6]. The latter is further supported by the fact that the fitted coefficients $c$ are condition dependent.

Analysing the aggregates in cells that are adapted to oxidative or salt stress, we found that stress typically leads to a higher number of slow or large aggregates compared to standard conditions. In addition, we could show that how cells deal with stress-induced aggregates differs between oxidative and salt stress. In NaCl, there is a stronger effect on the stoichiometries, while in $H_2O_2$ the decrease in the diffusion coefficient is more dominant. Since aggregates increase in stoichiometry while the number of aggregates per cell does not decline, we suggest that more misfolded proteins are being isolated thus subjected to the PQC. Moreover, in salt stress the total aggregate count per cell even increases, indicating that the cells could not adapt equally well as in oxidative stress.

Organising damaged or misfolded proteins in larger clusters can be a means to protect cells from further damage, since individual misfolded proteins are deleterious to cells, not only because they lose their function due to the loss of natural conformation, but also because the misfolding can result in a "toxic gain-of-function" [37]. Controlled aggregate formation can reduce the probability to cause further harm by decreasing the surface of reactive domains of misfolded proteins, by facilitating the spatial sequestering to confined spots in the cell and by reducing aggregate mobility [6, 36].

To better understand active mechanisms behind stress-induced aggregation, we studied ΔssCPY*-GFP aggregation of strains lacking or overexpressing Tsa1, one of the key players in the PQC network.

Tsa1 overexpression leads to a shift in the stochiometries towards larger aggregates, both in normal conditions and in oxidative stress. However, the numbers of aggregates per cell distinguish the two conditions. In standard conditions, we generally observed more foci per cell if Tsa1 is overexpressed. This not only shows that Tsa1 is involved in the collection and sequestering of aggregates, but also indicates that an increased amount of Tsa1 alone is not sufficient to remove aggregates from the system. Heat-shock proteins are especially important in this context and if not present, damage clearance is hindered [4, 36]. In $H_2O_2$, the overexpression results conversely to a decreased number of foci per cell. Thus, Tsa1, as a part of the full stress response, seems to facilitate protein aggregation as a precursor of clearance, leading to a more controlled way

of dealing with damage. Supporting this hypothesis, Tsa1 overexpression also correlates with small changes in the diffusion coefficients of large aggregates. In particular, large aggregates are slower in $H_2O_2$ stress, which was confirmed in a large absolute value of the fitted exponent ($|c| = 5.8$). In this microenvironment, due to the enhanced PQC, there are potentially more aggregates in inclusion bodies in spatially confined spots, such as JUNQ, IPOD and INQ, which are therefore highly restricted in their mobility. Tsa1 has been reported to be required for recognition of hydrogen peroxide-induced aggregates by sHsps [6]. Thus, our data may suggest that upon Tsa1 overexpression, more misfolded proteins are directed to and isolated within quality control sites. However, more microscopy data which would include fluorescently labelled INQ/JUNQ and IPOD is required to evaluate this hypothesis.

When Tsa1 is lacking, aggregates are, similar to Tsa1 overexpression, generally increased in size in standard and $H_2O_2$ condition, however the shift is less prominent. We could show that mainly fast aggregates are increased in stoichiometry. This could hint towards a reduction of controlled aggregation, such that ΔssCPY*-GFP clusters can still form, but rather by chance than active control. If two protein clusters of the same type collide it can be energy-efficient to aggregate together [40], and the probability for collisions is higher for fast molecules. Particularly in oxidative stress, large aggregates can exhibit comparably high diffusion coefficients and additionally there is a high number of aggregates in the majority of the analysed cells, emphasising the disruption of the PQC system caused by *tsa1Δ* [5, 41], that is not able to sequester and clear damage efficiently anymore.

Even though NaCl has not been connected to Tsa1 previously, we could show that if Tsa1 is lacking, there are often fewer aggregates per cell, which are furthermore usually smaller in size compared to the wildtype. Thus, our data suggest that the protein aggregation response to hyperosmotic stress is affected by Tsa1, potentially by NaCl-induced oxidative stress that activates Tsa1 [42, 43]. Counter-intuitively, the effect of *tsa1Δ* in salt stress appears to be beneficial for aggregate clearance. This underlines that cells likely deal differently with aggregates resulting from NaCl stress than those induced by $H_2O_2$, but further experiments are needed.

Slimfield microscopy that we used here is one of a multitude of super-resolution fluorescence imaging techniques. The most precise information regarding molecular behaviour can be achieved by further advancing and/or combining existing methods (reviewed in [44]). For example, MINFLUX is a variant of Stimulated Emission Depletion (STED) microscopy which uses the principle of selective stoichastic fluorophore switching (like PALM and STORM) and hence allows 1 nm precision of molecules 6 nm apart [45]. Moreover, a number of optical methods enabling 3D visualisation of individual molecules within living cells have also been developed (reviewed in [46]). However, fluorescent imaging requires appropriate tagging of the molecules of interest which may not only significantly affect their behaviour but also vary depending on a chosen fluorophore [47–49]. To overcome these limitations, super-resolution label-free approaches are being developed and successfully applied in studies of complex biological systems [50–53].

By acquiring detailed knowledge about biophysical properties of individual aggregates from single-molecule super-resolution microscopy data, we could gain insights in protein aggregation as a cellular response to exposure to oxidative and salt stress. While the analysis of this type of data alone reveals novel insights in aggregation formation and regulation, it also opens up new possibilities to build or complement mathematical models of protein aggregation with interesting applications in ageing and age-related diseases [54]. A major driver of ageing is the asymmetric distribution of damaged components between progeny and progenitor cells (retention) [55]. While mathematical models could show that the diffusion of aggregates of different size can establish this damage asymmetry in the budding yeast *S.cerevisiae* [31, 56–58], it is also known that more selective active processes are involved [59, 60]. By quantifying the properties of protein aggregates in a crowded cellular environment using single-molecule microscopy and feeding them into mathematical models, underlying mechanisms and the role of passive and active retention mechanisms in ageing can be explained more accurately. Furthermore, individual aggregate diffusion coefficients and their distributions from experiments can improve mathematical models of neurodegenerative diseases [61] by providing realistic parameters. Hence, single-molecule microscopy is a promising tool to further elucidate ageing through

mathematical modelling.

## CRediT authorship contribution statement

BS: Formal analysis, Software, Validation, Visualization, Writing original draft and revision; NW: Conceptualization, Data curation, Funding acquisition, Investigation, Project administration; ML: Resources, Writing revision; SS: Data curation, Formal analysis, Methodology, Project administration, Software, Supervision, Validation, Writing original draft and revision; MC: Conceptualization, Funding acquisition, Supervision, Writing revision.

## Declaration of competing interest

The authors declare no competing interests.

## Acknowledgements

This work was supported by the Swedish Research Council (VR2017-05117) and the Swedish Foundation for Strategic Research (FFL15-0238) to MC, Wilhelm och Martina Lundgrens vetenskapsfond to NW, the UK Engineering Physical Sciences Research Council (EP/T002166/1) and Leverhulme Trust (RPG-2019-156) to ML, and The Royal Society Newton International Fellowship (NF160208) to SS.

# References


1. López-Otín, C., Blasco, M. A., Partridge, L., Serrano, M. & Kroemer, G. The Hallmarks of Aging. *Cell* **153,** 1194–1217 (June 2013).
2. Ursini, F., Davies, K. J., Maiorino, M., Parasassi, T. & Sevanian, A. Atherosclerosis: another protein misfolding disease? *Trends in Molecular Medicine* **8,** 370–374 (Aug. 2002).
3. Moreau, K. L. & King, J. A. Protein misfolding and aggregation in cataract disease and prospects for prevention. *Trends in Molecular Medicine* **18,** 273–282 (May 2012).
4. Haslbeck, M., Franzmann, T., Weinfurtner, D. & Buchner, J. Some like it hot: the structure and function of small heat-shock proteins. *Nat Struct Mol Biol* **12,** 842–846 (Oct. 2005).
5. Hanzén, S. *et al.* Lifespan Control by Redox-Dependent Recruitment of Chaperones to Misfolded Proteins. *Cell* **166,** 140–151 (June 2016).
6. Hill, S. M., Hanzén, S. & Nyström, T. Restricted access: spatial sequestration of damaged proteins during stress and aging. *EMBO Rep* **18,** 377–391 (Mar. 2017).
7. Kaganovich, D., Kopito, R. & Frydman, J. Misfolded proteins partition between two distinct quality control compartments. *Nature* **454,** 1088–1095 (Aug. 2008).
8. Miller, S. B. *et al.* Compartment-specific aggregases direct distinct nuclear and cytoplasmic aggregate deposition. *EMBO J* **34,** 778–797 (Mar. 2015).
9. Schneider, K. L., Nyström, T. & Widlund, P. O. Studying Spatial Protein Quality Control, Proteopathies, and Aging Using Different Model Misfolding Proteins in S. cerevisiae. *Front. Mol. Neurosci.* **11,** 249 (July 2018).
10. Leake, M. C. The physics of life: one molecule at a time. *Phil. Trans. R. Soc. B* **368,** 20120248 (Feb. 2013).
11. Shashkova, S. & Leake, M. C. Systems biophysics: Single-molecule optical proteomics in single living cells. *Current Opinion in Systems Biology* **7,** 26–35 (Feb. 2018).
12. Plank, M., Wadhams, G. H. & Leake, M. C. Millisecond timescale slimfield imaging and automated quantification of single fluorescent protein molecules for use in probing complex biological processes. *Integr. Biol.* **1,** 602 (2009).
13. Reyes-Lamothe, R., Sherratt, D. J. & Leake, M. C. Stoichiometry and Architecture of Active DNA Replication Machinery in *Escherichia coli*. *Science* **328,** 498–501 (Apr. 2010).
14. Badrinarayanan, A., Reyes-Lamothe, R., Uphoff, S., Leake, M. C. & Sherratt, D. J. In vivo architecture and action of bacterial structural maintenance of chromosome proteins. *Science* **338,** 528–531 (Oct. 2012).
15. Stracy, M. *et al.* Single-molecule imaging of DNA gyrase activity in living Escherichia coli. *Nucleic Acids Res* **47,** 210–220 (Jan. 2019).
16. Syeda, A. H. *et al.* Single-molecule live cell imaging of Rep reveals the dynamic interplay between an accessory replicative helicase and the replisome. *Nucleic Acids Research* **47,** 6287–6298 (July 2019).
17. Wollman, A. J. M. & Leake, M. C. Millisecond single-molecule localization microscopy combined with convolution analysis and automated image segmentation to determine protein concentrations in complexly structured, functional cells, one cell at a time. *Faraday Discuss.* **184,** 401–424 (2015).
18. Sun, Y., Wollman, A. J. M., Huang, F., Leake, M. C. & Liu, L.-N. Single-Organelle Quantification Reveals Stoichiometric and Structural Variability of Carboxysomes Dependent on the Environment. *Plant Cell* **31,** 1648–1664 (July 2019).
19. Wollman, A. J. *et al.* Transcription factor clusters regulate genes in eukaryotic cells. *eLife* **6,** e27451 (Aug. 2017).

20. Wollman, A. J. M. *et al.* Single-molecule optical microscopy of protein dynamics and computational analysis of images to determine cell structure development in differentiating Bacillus subtilis. *Comput Struct Biotechnol J* **18,** 1474–1486 (2020).

21. Jin, X. *et al.* Membraneless organelles formed by liquid-liquid phase separation increase bacterial fitness. *Sci Adv* **7,** eabh2929 (Oct. 2021).

22. Miller, H. *et al.* High-Speed Single-Molecule Tracking of CXCL13 in the B-Follicle. *Front Immunol* **9,** 1073 (2018).

23. Cosgrove, J. *et al.* B cell zone reticular cell microenvironments shape CXCL13 gradient formation. *Nat Commun* **11,** 3677 (July 2020).

24. Stolz, A. & Wolf, D. H. *Ubiquitin Family Modifiers and the Proteasome: Reviews and Protocols* (eds Dohmen, R. J. & Scheffner, M.) 489–504 (Humana Press, Totowa, NJ, 2012).

25. Leake, M. C. *et al.* Stoichiometry and turnover in single, functioning membrane protein complexes. *Nature* **443,** 355–358 (Sept. 2006).

26. Armstrong, R. A. When to use the Bonferroni correction. *Ophthalmic Physiol Opt* **34,** 502–508 (Sept. 2014).

27. Shashkova, S., Andersson, M., Hohmann, S. & Leake, M. C. Correlating single-molecule characteristics of the yeast aquaglyceroporin Fps1 with environmental perturbations directly in living cells. *Methods* **193,** 46–53 (Sept. 2021).

28. Ma, H. *et al.* Thioredoxin and Glutaredoxin Systems Required for Oxidative Stress Resistance, Fungicide Sensitivity, and Virulence of Alternaria alternata. *Appl Environ Microbiol* **84** (ed Master, E. R.) (July 2018).

29. Luby-Phelps, K., Taylor, D. L. & Lanni, F. Probing the structure of cytoplasm. *The Journal of Cell Biology* **102,** 2015–2022 (June 1986).

30. Kumar, M., Mommer, M. S. & Sourjik, V. Mobility of Cytoplasmic, Membrane, and DNA-Binding Proteins in Escherichia coli. *Biophysical Journal* **98,** 552–559 (Feb. 2010).

31. Kinkhabwala, A., Khmelinskii, A. & Knop, M. Analytical model for macromolecular partitioning during yeast cell division. *BMC Biophys* **7,** 10 (Dec. 2014).

32. Erickson, H. P. Size and Shape of Protein Molecules at the Nanometer Level Determined by Sedimentation, Gel Filtration, and Electron Microscopy. *Biol Proced Online* **11,** 32–51 (Dec. 2009).

33. Stothard, P. The Sequence Manipulation Suite: JavaScript Programs for Analyzing and Formatting Protein and DNA Sequences. *BioTechniques* **28,** 1102–1104 (June 2000).

34. Dobson, C. M. Protein folding and misfolding. *Nature* **426,** 884–890 (Dec. 2003).

35. Labbadia, J. & Morimoto, R. I. The Biology of Proteostasis in Aging and Disease. *Annu. Rev. Biochem.* **84,** 435–464 (June 2015).

36. Tyedmers, J., Mogk, A. & Bukau, B. Cellular strategies for controlling protein aggregation. *Nat Rev Mol Cell Biol* **11,** 777–788 (Nov. 2010).

37. Lotz, G. P. & Legleiter, J. The role of amyloidogenic protein oligomerization in neurodegenerative disease. *J Mol Med* **91,** 653–664 (June 2013).

38. Minton, A. Confinement as a determinant of macromolecular structure and reactivity. *Biophysical Journal* **63,** 1090–1100 (Oct. 1992).

39. Rivas, G. & Minton, A. P. Macromolecular Crowding In Vitro , In Vivo , and In Between. *Trends in Biochemical Sciences* **41,** 970–981 (Nov. 2016).

40. Goodsell, D. S. & Olson, A. J. Structural Symmetry and Protein Function. *Annu. Rev. Biophys. Biomol. Struct.* **29.** Publisher: Annual Reviews, 105–153 (June 2000).

41. Weids, A. J. & Grant, C. M. The yeast Tsa1 peroxiredoxin protects against protein aggregate-induced oxidative stress. *Journal of Cell Science,* jcs.144022 (Jan. 2014).

42. AbdElgawad, H. *et al.* High Salinity Induces Different Oxidative Stress and Antioxidant Responses in Maize Seedlings Organs. *Front. Plant Sci.* **7** (Mar. 2016).

43. Jamnik, P., Medved, P. & Raspor, P. Increased glutathione content in yeastSaccharomyces cerevisiae exposed to NaCl. *Ann. Microbiol.* **56,** 175–178 (June 2006).

44. Shashkova, S. & Leake, M. C. Single-molecule fluorescence microscopy review: shedding new light on old problems. *Bioscience Reports* **37,** BSR20170031 (Aug. 2017).

45. Balzarotti, F. *et al.* Nanometer resolution imaging and tracking of fluorescent molecules with minimal photon fluxes. *Science* **355,** 606–612 (Feb. 2017).

46. Von Diezmann, L., Shechtman, Y. & Moerner, W. E. Three-Dimensional Localization of Single Molecules for Super-Resolution Imaging and Single-Particle Tracking. *Chem. Rev.* **117,** 7244–7275 (June 2017).

47. Schneider, K. L., Wollman, A. J. M., Nyström, T. & Shashkova, S. Comparison of endogenously expressed fluorescent protein fusions behaviour for protein quality control and cellular ageing research. *Sci Rep* **11,** 12819 (Dec. 2021).

48. Moore, I. & Murphy, A. Validating the Location of Fluorescent Protein Fusions in the Endomembrane System. *Plant Cell* **21,** 1632–1636 (June 2009).

49. Heppert, J. K. *et al.* Comparative assessment of fluorescent proteins for in vivo imaging in an animal model system. *MBoC* **27** (ed Strome, S.) 3385–3394 (Nov. 2016).

50. Qian, C. *et al.* Super-resolution label-free volumetric vibrational imaging. *Nat Commun* **12,** 3648 (Dec. 2021).

51. Ortega Arroyo, J. *et al.* Label-Free, All-Optical Detection, Imaging, and Tracking of a Single Protein. *Nano Lett.* **14,** 2065–2070 (Apr. 2014).

52. Ortega-Arroyo, J. & Kukura, P. Interferometric scattering microscopy (iSCAT): new frontiers in ultrafast and ultrasensitive optical microscopy. *Phys. Chem. Chem. Phys.* **14,** 15625 (2012).

53. Andrecka, J. *et al. Methods in Enzymology* 517–539 (Elsevier, 2016).

54. Santiago, E., Moreno, D. F. & Acar, M. Modeling aging and its impact on cellular function and organismal behavior. *Experimental Gerontology* **155,** 111577 (Nov. 2021).

55. Nyström, T. Spatial protein quality control and the evolution of lineage-specific ageing. *Phil. Trans. R. Soc. B* **366,** 71–75 (Jan. 2011).

56. Zhou, C. *et al.* Motility and Segregation of Hsp104-Associated Protein Aggregates in Budding Yeast. *Cell* **147,** 1186–1196 (Nov. 2011).

57. Andrade-Restrepo, M. Is Aggregate-Dependent Yeast Aging Fortuitous? A Model of Damage Segregation and Aggregate Dynamics. *Biophysical Journal* **113,** 2464–2476 (Dec. 2017).

58. Song, R. & Acar, M. Stochastic modeling of aging cells reveals how damage accumulation, repair, and cell-division asymmetry affect clonal senescence and population fitness. *BMC Bioinformatics* **20,** 391 (Dec. 2019).

59. Liu, B. *et al.* Segregation of Protein Aggregates Involves Actin and the Polarity Machinery. *Cell* **147,** 959–961 (Nov. 2011).

60. Paoletti, C., Quintin, S., Matifas, A. & Charvin, G. Kinetics of Formation and Asymmetrical Distribution of Hsp104-Bound Protein Aggregates in Yeast. *Biophysical Journal* **110,** 1605–1614 (Apr. 2016).

61. Andrade-Restrepo, M., Ciuperca, I. S., Lemarre, P., Pujo-Menjouet, L. & Tine, L. M. A reaction–diffusion model of spatial propagation of A$\beta $ oligomers in early stage Alzheimer's disease. *J. Math. Biol.* **82,** 39 (Apr. 2021).

# The effect of stress on biophysical characteristics of misfolded protein aggregates in living *Saccharomyces cerevisiae* cells

## Supplementary Information

Barbara Schnitzer [1,2], Niek Welkenhuysen [1,2], Mark C. Leake [3,4], Sviatlana Shashkova [1,2,3,§], Marija Cvijovic [1,2]

corresponding authors: marija.cvijovic@chalmers.se and sviatlana.shashkova@gu.se

[1] Department of Mathematical Sciences, Chalmers University of Technology, 412 96 Gothenburg, Sweden

[2] Department of Mathematical Sciences, University of Gothenburg, 412 96 Gothenburg, Sweden

[3] Department of Physics, University of York, YO10 5DD York, UK

[4] Department of Biology, University of York, YO10 5DD York, UK

[§] Current address: Department of Physics, University of Gothenburg, 412 96 Gothenburg, Sweden

**File S1: Stoichiometries and diffusion coefficients of all measured aggregates.**

**File S2: Collection of all calculated p values.**

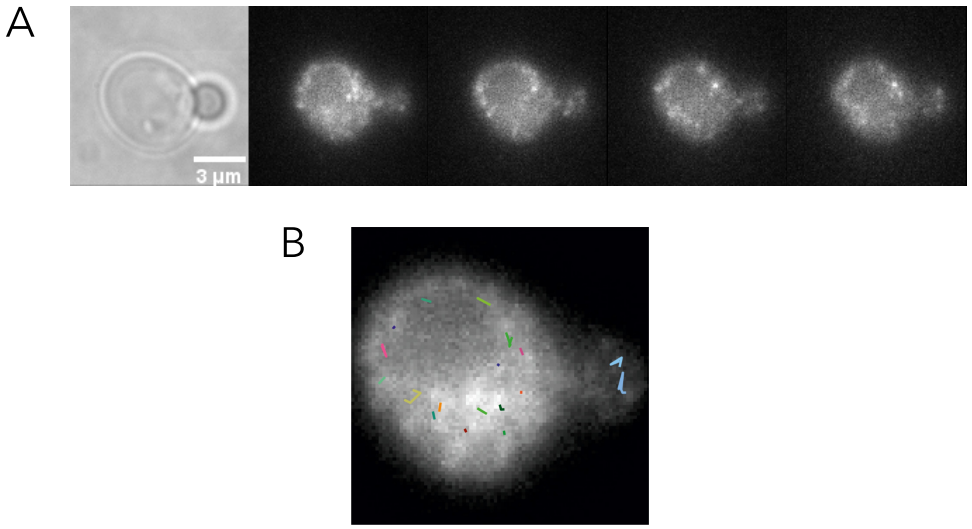


**Figure S1: Tracking of aggregates from microscopy images.** (A) Example microscopy images for several successive time points (5ms intervals). (B) Corresponding trajectories of aggregates found by the algorithm. The image is the sum of the images where tracks were found.

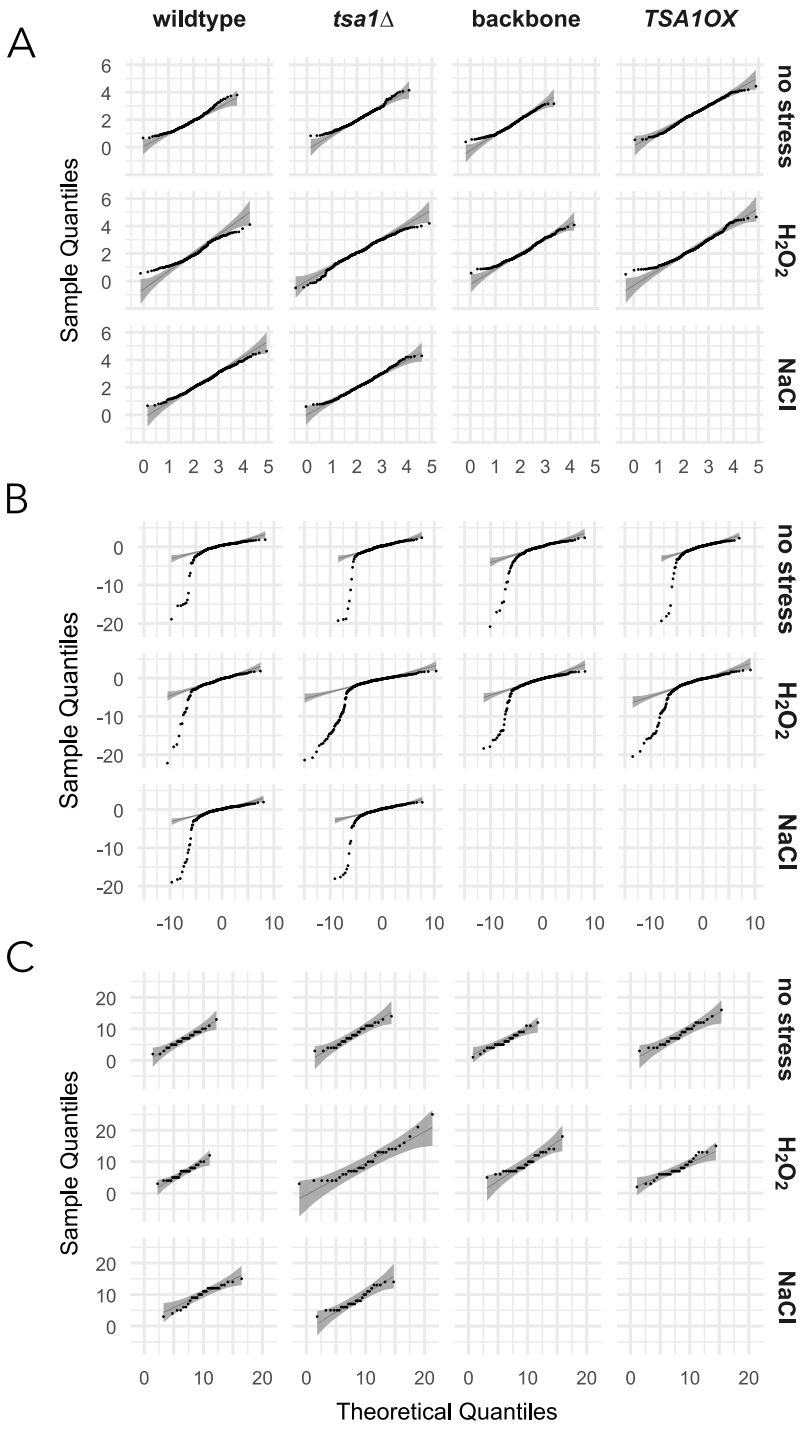


**Figure S2: Normality check via QQ plots.** (A) QQ plot under the assumption that the stoichiometries $S$ are log-normally distributed, i.e. the logarithms of $S$ are normally distributed. There are abnormal tails in both extremes in many of the conditions, and log-normality cannot be assumed. (B) QQ plot under the assumption that the diffusion coefficients $D$ are log-normally distributed, i.e. the logarithms of $D$ are normally distributed. The distributions are skewed with heavy tails towards low $D$, and log-normality cannot be assumed. (C) QQ plot under the assumption that the aggregate counts per cell are normally distributed. The data can be considered normally distributed.

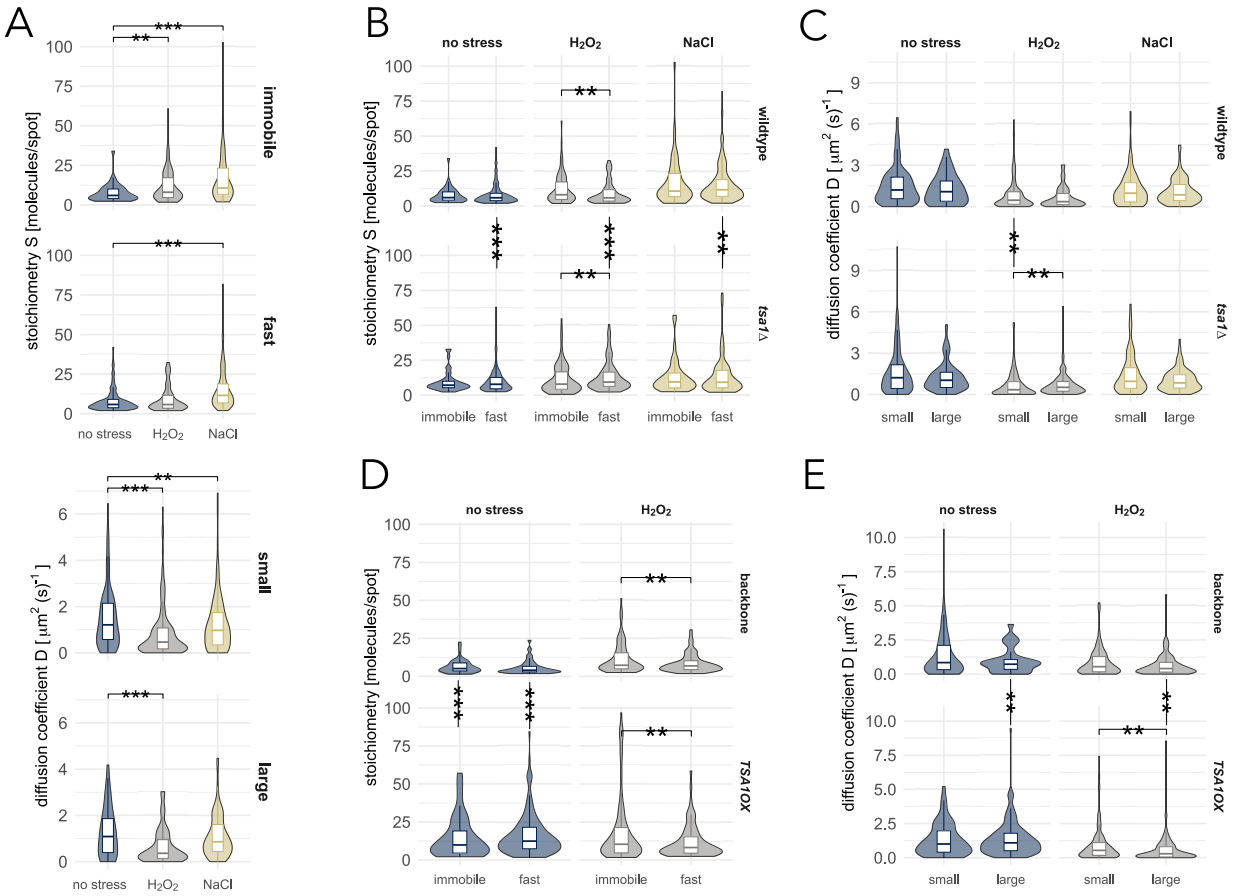


**Figure S3: Distinction between subpopulation.** (A) Distributions (violin with integrated boxplot) of the aggregate stoichiometry $S$ for immobile ($D < 0.3\mu m^2(s)^{-1}$) and fast ($D > 0.8\mu m^2(s)^{-1}$) aggregates (upper panel), as well as for small ($S < 10$) and large ($S \geq 10$) aggregates (lower panel), in standard conditions and under stress. Immobile and fast aggregates react different to stress in $H_2O_2$. Small and large aggregates react different to stress in NaCl instead. (B-C) Same distributions of the subpopulations for the wildtype compared to Tsa1 deletion (*tsa1Δ*), which significantly affects fast aggregates (no stress $p = 0.002$, $H_2O_2$ $p < 0.0001$, NaCl $p = 0.024$), but not immobile ones. In oxidative stress, it is even possible to distinguish the two subpopulations within a data set. Fast aggregates are generally smaller than immobile aggregates in the wildtype ($p = 0.012$), but *tsa1Δ* in this condition leads to a reversed trend and fast aggregates increase in stoichiometry compared to immobile aggregates ($p = 0.012$). (D-E) Same distributions of the subpopulations for the overexpression backbone compared to Tsa1 overexpression (*TSA1OX*). In this case, immobile and fast aggregates seem to be equally affected by *TSA1OX*. However, there is a difference between $D$ for large aggregates. In non-stressed conditions large aggregates can reach higher $D$ ($p = 0.036$), while they are more restricted in their mobility in $H_2O_2$ ($p = 0.028$). The latter leads to a more clear distinction between distributions of small and large aggregates when Tsa1 is overexpressed ($p = 0.006$).

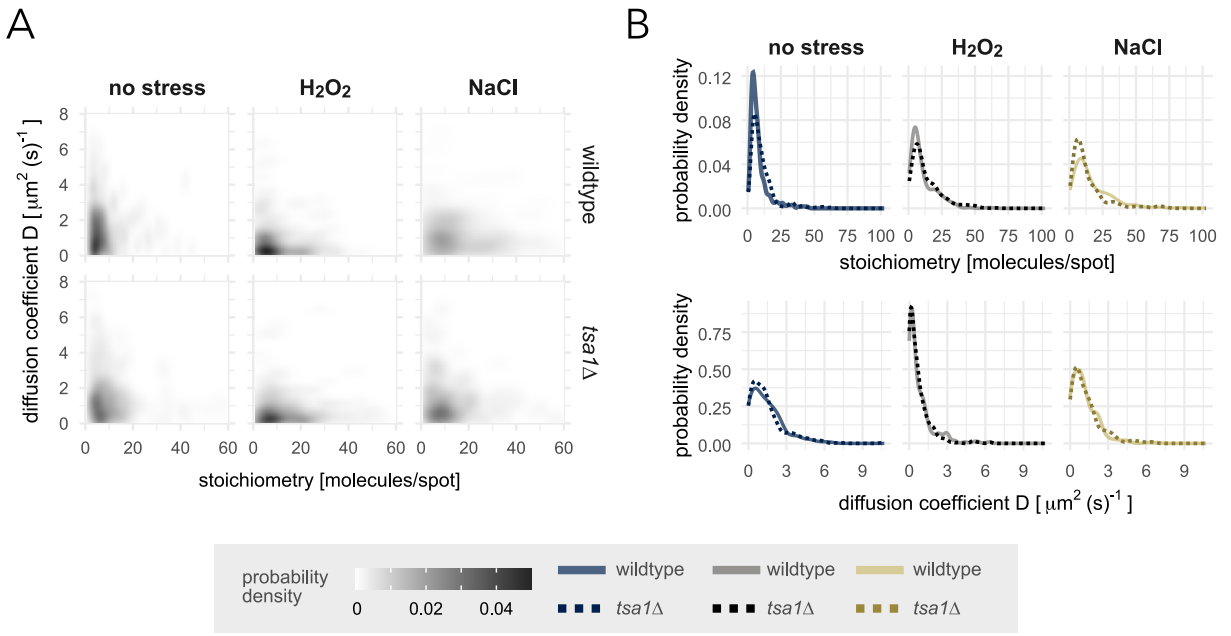


**Figure S4: Complementary plots for the comparison between wildtype and Tsa1 deletion (*tsa1Δ*).** 2-d (A) and 1-d (B) probability densities of the aggregate stoichiometry $S$ and the diffusion coefficient $D$.

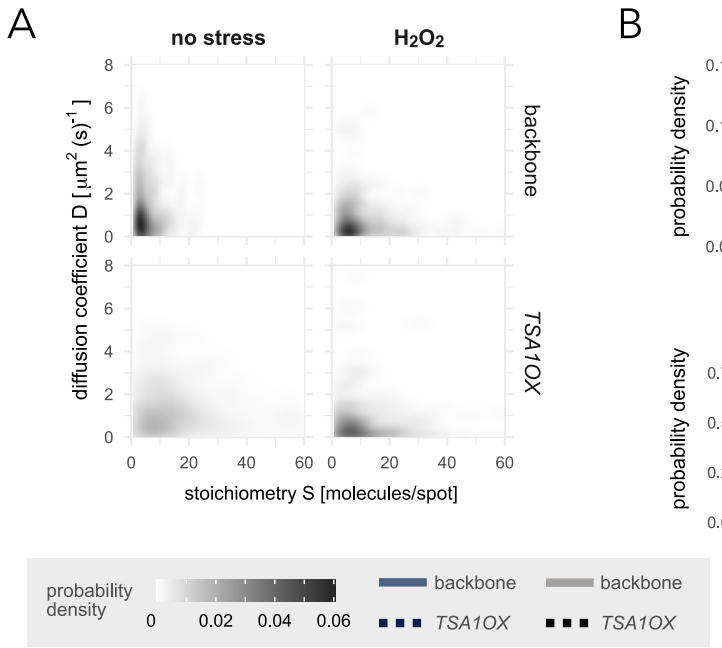


**Figure S5: Complementary plots for the comparison between backbone and Tsa1 overexpression (*TSA1OX*).** 2-d (A) and 1-d (B) probability densities of the aggregate stoichiometry $S$ and the diffusion coefficient $D$.

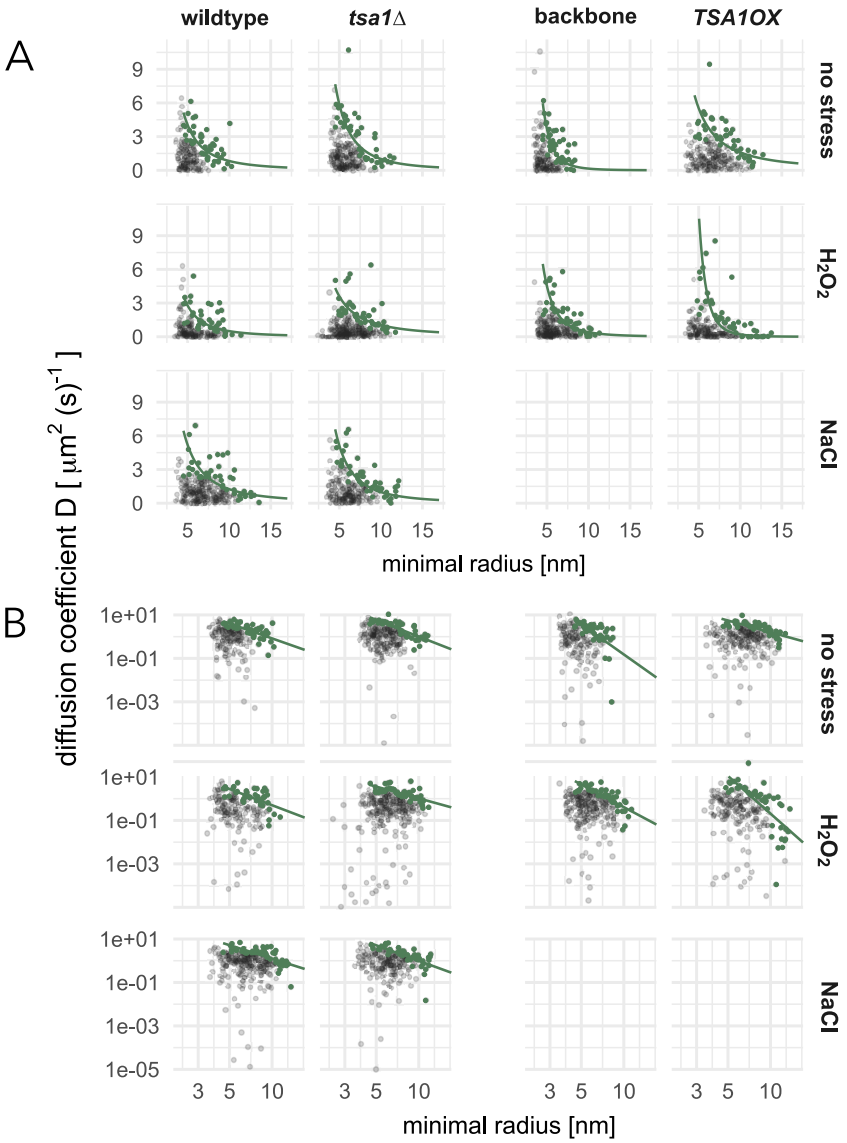


**Figure S6: Data with exponential fits $D(r)$.** All data sets with a reduced data set marked in green, consisting of the maximal measured diffusion coefficients per stoichiometry interval (10 intervals for $S > 4$ with the 5 largest $D$ per interval), with normal axis (A) and in log-log scale (B). The reduced data set is used for fitting the function $D(r) = D_0 \cdot \exp(\alpha r)$. The fit becomes a linear regression problem in the log-log scale. The stoichiometry of the aggregate was converted to a minimal radius by (1) and (2) according to [32].